# Development of a piezo-driven 3-DOF stage with T-shape flexible hinge mechanism

Kunhai Cai[1], Yanling Tian[1], Fujun Wang[1], Dawei Zhang[1], Bijan Shirinzadeh[2]

[1]Key Laboratory of Mechanism Theory and Equipment Design of Ministry of Education, Tianjin University, Tianjin 300072, China

[2]Robtics and Mechatronics Research Laboratory, Department of Aerospace and Mechanical Engineering, Monash University, VIC 3800, Australia

**Abstract**: This paper presents a 3-DOF (Degree of freedom) stage with T-shape flexible hinge mechanism for the applications in the precision measurement equipments and micro/nano manipulation systems. The stage is driven by three piezoelectric actuators (PEAs) and guided by a flexible hinge based mechanism with three symmetric T-shape hinges. The proposed T-shape flexible hinge mechanism can provide excellent planar motion capability with high stability, and thus guarantee the outstanding dynamics characteristics. The theoretical modeling of the stage was carried out and the stiffness and the dynamic resonance frequency have been obtained. The kinematic model of the 3-DOF stage was established and the workspace has been analyzed. The characteristics of the stage were investigated using finite element analysis (FEA). Experiments were conducted to examine the performance of the stage, through this stage, X-axis translational motion stroke of 6.9 μm, Y-axis translational motion stroke of 8.5 μm and rotational motion stroke along Z-axis of 289 μrad can be achieved. A hybrid feedforward/feedback control methodology has been proposed to eliminate the nonlinear hysteresis, the trajectory tracking performances and to reduce external disturbance of the 3-DOF stage.

**Keywords**: Stage, Piezoelectric actuators, Flexible hinge mechanism

## 1. Introduction

The roles of precision positioning technology have become increasingly important in various industry fields, such as micro/nano manipulation system, microelectronics processing, optical instruments and measurement systems. A precision positioning system mainly composed of actuation device, guide mechanism and end effector. The guide mechanism is one of the key factors to determine the static and dynamic performance of the positioning system. In order to guarantee positioning accuracy, one of the best choices is to utilized flexure based mechanism for guidance of the motion. The flexure based mechanism is capable of improving the motion accuracy due to the advantages of flexure hinges including no backlash, free of wear, no lubrication, and low friction.

Several studies have focused on the design and control of precision positioning systems with flexure-based mechanisms. In order to improve the motion accuracy, there are a variety of flexure hinges have been proposed and utilized in the positioning system, including notch-type hinge [1-3], leaf-spring hinge [4-6], right elliptical hinge [7], V-shape flexure hinge[8], cross-axis flexural pivots [9-11], split-tube flexural pivots [12], cartwheel hinges [13-17], and so on. Among the proposed flexure hinges, the notch-type hinge and leaf-spring hinge are the most popular and widely utilized in precision positioning system. Particularly, the leaf-spring hinges possess the capability of large working range.

Recent research efforts have been directed towards the development of high performance positioning mechanisms for bio-nanotechnology, AFM (atomic force microscope) and confocal microscopes [18-20]. These advanced applications bring a number of tremendous challenges for the mechanical design and optimization of positioning mechanisms. In order to implement the positioning and orientation of the sample for the precision measurement and characterisation, it is

necessary to develop a 3-DOF positioning stage which can be utilized to conduct the in-plane motion. Tian et al. have designed a 3-DOF flexure-based mechanism for micro/nano manipulation [21]. In order to improve the stiffness of the moving platform, a monolithic flexure-based 3-RRR parallel mechanism is utilized to implement planar motions. Hwang et al. presented a novel ultra-precision in-plane XYθ positioning stage with kinematic decoupling between translational motion and rotational motion components [22], Qin et al. proposed the design of a novel 3-DOF monolithic manipulator with three improved Scott-Russell (ISR) mechanisms [23]. In these developed mechanisms, a series of the notch-type hinges have been adopted as a guide mechanism. However, the mechanical design of the 3-DOF positioning system with combination of the notch type and leaf-spring hinges has also been provided by Kim et al.[24] and Bhagat et al.[25]. In addition, Kim et al. presented the mechanical design of a 3-DOF flexure-based parallel compliant mechanism for the hollow type biomedical specimen stage base on notch-type hinges and cartwheel hinges [26].

This paper presents a novel 3-DOF precision positioning stage featured with three symmetric T-shape flexure hinges design. The T-shape flexure hinge is composed of three leaf-spring hinge subsections connected at the together like a T-joint. Thus, the T-shape flexure hinge can provide the in plane motion with relatively large out-of-plane stiffness, and meanwhile the proposed T-shape flexure hinge has the capability of compact structural design for such kinds of micro/nano positioning stages. It is demonstrated from the computational analyses that the proposed T-shape flexure hinge can provide high natural frequency, large working range and high motion dexterity. The mechanical design of the flexure-based mechanism using parallel motion and actuation configuration is provided. The monolithic mechanism is manufactured using the WEDM technique

to guarantee the machining accuracy and motion precision. The analytical models of the developed mechanism have been established to investigate the static and dynamic characteristics of the entire system. Both the stiffness and working space of the moving platform have been analyzed. The FEA (finite element analyse) has also been conducted to obtain further insights into the performance of the developed flexure-based mechanism. A number of experiments have been performed to verify the established models and characteristics of the flexure-based mechanism. This paper is organized as follows: Section II introduces mechanical design of the stage, and analytic models have established in section III. Section IV provides the kinematic analysis of the stage. In Section V, FEA has been performed to validate the static and dynamic characteristics of the flexure-based mechanism. The experimental setup and results have been provided in section VI. Conclusions are presented in Section VII.

## 2. Mechanical design

The solid model of the 3-DOF stage is shown in Fig.1. The parallel driven configuration is utilized in the design. It can be seen that the stage is mainly composed of three piezoelectric actuators (PEAs), three T-shape flexure hinge mechanisms, a moving platform and a base. Three T-shape flexure hinge mechanisms are located at the circle with the separation angle of 120 °. Each T-shape flexure hinge mechanism consists of three leaf-spring hinge subsections connected at the together like a T-joint as shown in Fig. 2. One end of each T-shape flexure hinge mechanism is connected to the moving platform and the other ends fixed on the base. On the same circumference of the T-shape flexure hinge mechanism, there are three slots to install PEAs with the separation angle of 120 °. Each slot separates from the T-shape flexure hinge mechanism with an angle of 60 °. The PEA can be preloaded through the behind fine screw bolt. Through simultaneously controlling

the PEAs, the moving platform can implement the translations in the X and Y directions, and rotation about Z axis. Because the performance of guide mechanism has significant influence on the characteristics of the stage, the dynamic characteristic of the T-shape flexure hinge mechanism is firstly examined. Modal analysis is performed to examine the dynamic characteristics of the T-shape flexure hinge mechanism using finite element analysis package ANSYS software. The boundary conditions for simulation are chosen as: The outer edges of the both hinges I and II are fixed and constrained for all degrees of freedom, as shown in Fig. 3(a). The first three vibration mode shapes are obtained and shown in Fig. 3. It can be seen that only the leaf-spring hinge III vibrates in the X direction in the first vibration mode shape, the hinges I and II rotate about the X axis in the second vibration mode shape, and the hinges I and II vibrate in the Z axis in the third vibration mode shape. In order to guarantee excellent static and dynamic characteristics of the 3-DOF flexure stage, some undesired motion of T-shape flexure hinge mechanism should be avoided, such as the second mode shape, which can cause the instability of the stage system. Thus, the three T-shape flexure hinge mechanism are symmetrically arranged in the same circle to form the parallel supporting mechanism. In this configuration, the undesired vibration mode shape of the T-shape flexure hinge mechanism can be overcome.

**3 Stiffness modeling**

According to the Hooke's law, the relationship between the displacement and applied force of the flexure hinge can be expressed by

$$F = KQ \tag{1}$$

where $\boldsymbol{K}$ is the stiffness matrix, $Q = [\Delta x \quad \Delta y \quad \Delta z \quad \theta x \quad \theta y \quad \theta z]^T$, and $F = [Fx \quad Fy \quad Fz \quad Mx \quad My \quad Mz]^T$.

The compliance matrix $\boldsymbol{C}$ can be expressed as

$$C = \begin{bmatrix} C_{Fx}^{\Delta x} & 0 & 0 & 0 & 0 & 0 \\ 0 & C_{Fy}^{\Delta y} & 0 & 0 & 0 & C_{Mz}^{\Delta y} \\ 0 & 0 & C_{Fz}^{\Delta z} & 0 & C_{My}^{\Delta z} & 0 \\ 0 & 0 & 0 & C_{Mx}^{\theta x} & 0 & 0 \\ 0 & 0 & C_{Fz}^{\theta y} & 0 & C_{My}^{\theta y} & 0 \\ 0 & C_{Fy}^{\theta z} & 0 & 0 & 0 & C_{Mz}^{\theta z} \end{bmatrix} \tag{2}$$

The compliance matrix of the leaf-spring hinge shown in Fig. 4 can be obtained as [27]

$$C^{h} = \begin{bmatrix} \frac{l}{Ebt} & 0 & 0 & 0 & 0 & 0 \\ 0 & \frac{4l^3}{Ebt^3} + \frac{l}{Gbt} & 0 & 0 & 0 & \frac{6l^2}{Ebt^3} \\ 0 & 0 & \frac{4l^3}{Eb^3t} + \frac{l}{Gbt} & 0 & -\frac{6l^2}{Eb^3t} & 0 \\ 0 & 0 & 0 & \frac{l}{Gk_2bt^3} & 0 & 0 \\ 0 & 0 & -\frac{6l^2}{Eb^3t} & 0 & \frac{12l}{Eb^3t} & 0 \\ 0 & \frac{6l^2}{Ebt^3} & 0 & 0 & 0 & \frac{12l}{Ebt^3} \end{bmatrix} \tag{3}$$

where $E$ is the elastic modulus, $G$ is the shear modulus, and $k_2=b/t$ is the geometric parameter.

For the T-shape flexure hinge mechanism composed of three leaf-spring hinges, a global coordinate system $O$-$XYZ$, and three local coordinate systems $O_1$-$X_1Y_1Z_1$, $O_2$-$X_2Y_2Z_2$ and $O_3$-$X_3Y_3Z_3$ are established and shown in Fig. 5, the local coordinate system $O_3$-$X_3Y_3Z_3$ coincides with the global coordinate system $O$-$XYZ$. $\boldsymbol{C^o}$ is the compliance matrix of the leaf-spring hinge in the global coordinate system $O$-$XYZ$, $\boldsymbol{C^h}$ represents the compliance matrix of the leaf-spring hinge in the local coordinate system, and $\boldsymbol{T}$ is a transformation matrix between the local coordinate system to the global coordinate system. Therefore

$$C^{o} = TC^{h}T^{T} \tag{4}$$

$$T = \begin{bmatrix} R & 0 \\ 0 & R \end{bmatrix} \begin{bmatrix} E & \phi(r) \\ 0 & E \end{bmatrix} \tag{5}$$

$$\phi(r) = \begin{bmatrix} 0 & -r_z & r_y \\ r_z & 0 & -r_x \\ -r_y & r_x & 0 \end{bmatrix} \tag{6}$$

where $\boldsymbol{T}$ is a (6×6) matrix, $\boldsymbol{R}$ is rotational transformation matrix with the size of (3×3), the matrix $\boldsymbol{E}$ has the size of (3×3), and $\phi(r)$ is the position vector which local coordinate system of the hinge in the global coordinate system, $[r_x, r_y, r_z]^T$ represents the vector $\boldsymbol{r}$ expressed in the global coordinate system.

The T-shape hinge compliance matrix can be calculated as

$$C_T = [(C_1^o)^{-1} + (C_2^o)^{-1}]^{-1} + C_3^o \tag{7}$$

According to the above analysis, introducing $\boldsymbol{T}^i$ ($i$=1, 2), a transformation matrix from the local coordinate fixed to the hinge $i$ of the global coordinate, also the rotational transformation matrix $\boldsymbol{R}^i$ ($i$=1, 2) and the position vector $\phi^i(r)$ ($i$=1, 2) given by Eq.(8) and (9), respectively.

$$T^1 = \begin{bmatrix} R^1 & 0 \\ 0 & R^1 \end{bmatrix} \begin{bmatrix} E & \phi^1(r) \\ 0 & E \end{bmatrix} \tag{8}$$

$$T^2 = \begin{bmatrix} R^2 & 0 \\ 0 & R^2 \end{bmatrix} \begin{bmatrix} E & \phi^2(r) \\ 0 & E \end{bmatrix} \tag{9}$$

where $R^1 = \begin{bmatrix} 0 & -1 & 0 \\ 1 & 0 & 0 \\ 0 & 0 & 1 \end{bmatrix}$, $\phi^1(r) = \begin{bmatrix} 0 & 0 & \frac{(L+t)}{2} \\ 0 & 0 & -\frac{t}{2} \\ \frac{(L+t)}{2} & -\frac{t}{2} & 0 \end{bmatrix}$, $R^2 = \begin{bmatrix} 0 & 1 & 0 \\ -1 & 0 & 0 \\ 0 & 0 & 1 \end{bmatrix}$, and

$\phi^2(r) = \begin{bmatrix} 0 & 0 & \frac{(L+t)}{2} \\ 0 & 0 & \frac{t}{2} \\ -\frac{(L+t)}{2} & -\frac{t}{2} & 0 \end{bmatrix}$.

Then the stiffness matrix of the T-shape hinge in global coordinate is obtained and given as follows:

$$K_T = C_T^{-1} \tag{10}$$

Figure 6 shows the T-shape flexure hinge based mechanism. From dynamics point of view, the proposed 3-DOF stage can be modeled as an in-plane multi spring-mass system. The T-shape flexure hinge can be considered as a spring, and the moving platform is equivalent to a dumped mass. Thus, based on the Newton's motion law, the dynamic model of the developed 3-DOF flexure-based stage can be given as follows:

$$M\ddot{X} + KX = F \tag{11}$$

where $M = diag\begin{bmatrix} m & m & I_z \end{bmatrix}$, $K = diag\begin{bmatrix} K_x & K_y & K_\varphi \end{bmatrix}$, $F = \begin{bmatrix} f_x & f_y & M_z \end{bmatrix}^T$, $X = \begin{bmatrix} x & y & \varphi \end{bmatrix}^T$, $M$, $K$, and $F$ are the mass matrix, stiffness matrix and force vector of the system, respectively.

The stiffness of the stage can be calculated by

$$K = \sum_{j=0}^{3} R_j K_{Tj} R_j^T \tag{12}$$

where $\boldsymbol{R}_j$ is the rotational transformation matrix from the local coordinate $O_j$-$X_jY_j$ fixed to the T-shape flexure hinge $j$ of the global coordinate $O$-$XY$ as shown in Fig. 6, and given by

$$R_1 = \begin{bmatrix} \cos 0 & -\sin 0 & 0 \\ \sin 0 & \cos 0 & 0 \\ 0 & 0 & 1 \end{bmatrix}, R_2 = \begin{bmatrix} \cos\theta & \sin\theta & 0 \\ -\sin\theta & \cos\theta & 0 \\ 0 & 0 & 1 \end{bmatrix}, R_3 = \begin{bmatrix} \cos\theta & -\sin\theta & 0 \\ \sin\theta & \cos\theta & 0 \\ 0 & 0 & 1 \end{bmatrix}$$

If the second-order term in Eq. (11) is ignored, the static displacements of moving platform can be calculated from the stiffness matrix and the input force vector:

$$KX = F \tag{17}$$

The resonance frequencies of the 3-DOF stage can be obtained by solving the following equation.

$$\left| K - w^2 M \right| = 0 \tag{18}$$

## 4. Workspace analysis

Figure 7 shows the geometry schematic diagram of the 3-DOF stage. $A_1$, $B_1$ and $C_1$ are the contact points between the PEAs and the moving platform, and the a geometric model of the stage can be simplified as a triangle *ABC* with three driving levers *A*-$A_1$, *B*-$B_1$ and *C*-$C_1$. As shown in Fig.7(a), a reference coordinate *O-XY* is established as global frame. A moving coordinate frame *O*'-*X*'*Y*' is fixed on the moving platform as shown in Fig.7(b). In the coordinate *O-XY*, the coordinates of points *O*, *A* and $A_1$ are (0,0), (*R*, 0) and (*R*,-*L*), respectively. When the PEA drives the lever *A*-$A_1$, the position of the center *O* move to *O*' whose coordinate is ($x$, $y$, $\alpha$) and the points *A* and $A_1$ moves to points *A*' and $A_1$', respectively.

As shown in Fig.7, a circular flexible hinge is used to model the contact between the PEA and the moving platform, and thus it can ensure that the PEA contacts with the moving platform during motion process, meanwhile allowing relatively rotation deformation between them.

The coordinate of points *A*' and $A_1$' in the coordinate *O-XY* can be respectively given as follows:

$$(A'_x, A'_y) = (x + R\cos\alpha, y + R\sin\alpha) \tag{19}$$

$$(A_1'_x, A_1'_y) = (A'_x + L\sin\beta, A'_y - L\cos\beta) \tag{20}$$

Thus

$$A_1'_x = A'_x + L\sin\beta = A_{1x} = R \tag{21}$$

And

$$\sin\beta = \frac{R - A'_x}{L} = \frac{R(1-\cos\alpha) - x}{L}$$

$$(A_1'_x, A_1'_y) = \{R, y + R\sin\alpha - \sqrt{L^2 - [R(1-\cos\alpha) - x]^2}\}$$

Therefore, the relationship between the elongation of the PEA-A ($\delta_{A1'\text{-}A1}$) and the output of the

moving platform can be given as follows:

$$\delta_{A1'-A1} = \left\| A1' - A1 \right\| = L + y + R\sin\alpha - \sqrt{L^2 - [R(1-\cos\alpha) - x]^2} \tag{22}$$

Similarly, the following equations are obtained.

$$\delta_{B1'-B1} = L + \left( -\frac{y}{2} - \frac{\sqrt{3}}{2}x \right) + R\sin\alpha - \sqrt{L^2 - [R(1-\cos\alpha) - (\frac{\sqrt{3}}{2}y - \frac{x}{2})]^2} \tag{23}$$

$$\delta_{C1'-C1} = L + \left( -\frac{y}{2} + \frac{\sqrt{3}}{2}x \right) + R\sin\alpha - \sqrt{L^2 - [R(1-\cos\alpha) - (-\frac{\sqrt{3}}{2}y - \frac{x}{2})]^2} \tag{24}$$

Rewriting the above equations into matrix form, the following relationship can be obtained:

$$\begin{bmatrix} \delta_{A1'-A1} \\ \delta_{B1'-B1} \\ \delta_{C1'-C1} \end{bmatrix} = T \begin{bmatrix} x \\ y \\ \alpha \end{bmatrix} \tag{25}$$

where

$$T = \begin{bmatrix} \frac{\partial(\delta_{A1'-A1})}{\partial x} & \frac{\partial(\delta_{A1'-A1})}{\partial y} & \frac{\partial(\delta_{A1'-A1})}{\partial \alpha} \\ \frac{\partial(\delta_{B1'-B1})}{\partial x} & \frac{\partial(\delta_{B1'-B1})}{\partial y} & \frac{\partial(\delta_{B1'-B1})}{\partial \alpha} \\ \frac{\partial(\delta_{C1'-C1})}{\partial x} & \frac{\partial(\delta_{C1'-C1})}{\partial y} & \frac{\partial(\delta_{C1'-C1})}{\partial \alpha} \end{bmatrix} \tag{26}$$

The initial value (0,0,0) is substituted into Equation (26), therefore

$$\frac{\partial(\delta_{A1'-A1})}{\partial x}\Big|_{(0,0,0)} = 0 \qquad \frac{\partial(\delta_{A1'-A1})}{\partial y}\Big|_{(0,0,0)} = 1 \qquad \frac{\partial(\delta_{A1'-A1})}{\partial \alpha}\Big|_{(0,0,0)} = R$$

$$\frac{\partial(\delta_{B1'-B1})}{\partial x}\Big|_{(0,0,0)} = -\frac{\sqrt{3}}{2} \qquad \frac{\partial(\delta_{B1'-B1})}{\partial y}\Big|_{(0,0,0)} = -\frac{1}{2} \qquad \frac{\partial(\delta_{B1'-B1})}{\partial \alpha}\Big|_{(0,0,0)} = R$$

$$\frac{\partial(\delta_{C1'-C1})}{\partial x}\Big|_{(0,0,0)} = \frac{\sqrt{3}}{2} \qquad \frac{\partial(\delta_{C1'-C1})}{\partial y}\Big|_{(0,0,0)} = -\frac{1}{2} \qquad \frac{\partial(\delta_{C1'-C1})}{\partial \alpha}\Big|_{(0,0,0)} = R$$

The relationship between output displacement and input displacement can be expressed as

$$\begin{bmatrix} x \\ y \\ \alpha \end{bmatrix} = T^{-1} \begin{bmatrix} \delta_{A1'-A1} \\ \delta_{B1'-B1} \\ \delta_{C1'-C1} \end{bmatrix} \tag{27}$$

where $\boldsymbol{T}^{-1}$ is a kinematics matrix,

$$T^{-1} = \begin{bmatrix} 0 & \frac{1}{\sqrt{3}} & -\frac{1}{\sqrt{3}} \\ \frac{2}{3} & -\frac{1}{3} & -\frac{1}{3} \\ \frac{1}{3R} & \frac{1}{3R} & \frac{1}{3R} \end{bmatrix} \tag{28}$$

Based on the specification of the PEA, the working stroke is set as 12 μm, and thus the workspace of the stage have been calculated and shown in Fig. 8.

## 5 Finite element analyses

Finite element analysis is conducted to validate the established models and obtain further insights into the static and dynamic characteristics of the developed flexure-based mechanism. The commercial finite element software ANSYS is utilized to perform the analyses. The finite element model of the stage is shown in Fig.9. In order to improve the computational accuracy, the mapping mesh method is adopted. The mesh is strictly controlled in the areas of flexure hinges, where the large deformation is generally occurred.

### 5.1 Static analyses

In order to obtain the motion characteristics of the moving platform, the static characteristic analysis is carried out through arranging the different working style of the driven PEAs and the analysis results are shown in Figure 10. Fig. 10(a) shows that when only one PEA works, the working area of the movable platform will move along X- and Y- axes, while rotating around one axis. Fig. 10(b) shows that when two PEAs work together, the working area will also move along X- and Y- axis, while rotating around one axis which is closer to the Z axis. In Figure 10(c), it shows that the working area has only pure rotation about the Z axis. From the above analysis, it can be seen that the motion of the 3-DOF stage is coupled between the three motion directions.

When three PEAs work together with maximum elongation 15 μm, the stresses of the hinges are observed in Fig. 11. It is noted that the maximum stress of the hinges is 58 MPa, which is much smaller than the yield strength of material (434 MPa). This indicates that the T shape flexure hinge can provide more high working range, if it is driven by larger stroke actuators.

Through data processing of the FEA result, we can obtain the matrix $\boldsymbol{T}^{-1}$.

$$T^{-1} = \begin{bmatrix} 0.001 & -0.62827 & 0.6271 \\ -0.72547 & 0.3611 & 0.3640 \\ 1.0498\times10^{-5} & 1.0386\times10^{-5} & 1.0395\times10^{-5} \end{bmatrix}$$

Fig. 12 shows the output displacement of the stage when the PEA-B works only. The output displacement of the stage by FEA simulation is larger than the theoretical value which is due to the assumption made in the kinematics analysis of the stage. The maximum working range of the moving platform is given in Table I. The stiffness of the 3-DOF are also calculated based on the FEA results, and compared with the theoretical analyses, as shown in Table II. It is noted that the FEA results is in good agreement with the theoretical computation. This indicates that the analytical models are correct and can be used for the static and dynamic analyses of the developed flexure based stage.

**5.2 Dynamic analyses**

The dynamic characteristics of the stage are investigated through the modal analysis and the results are shown in Fig. 13. As is shown in Fig.13(a) the first mode shows that the stage rotates about the Z-axis, and the corresponding frequency is 528.11Hz. In the second and third vibration modes the stage moves in the Y-axis and X-axis, respectively, and the corresponding frequencies are 626.92 Hz and 626.95 Hz, respectively. If the PEAs are installed, it can be realized by incorporating spring-damper components into the stage. It is considered as a spring with a constant stiffness *k*, one

end of the spring is fixed and the other end is attached on the moving platform. The simulation results show that the first three natural frequencies increase to 786.04 Hz, 787.13 Hz and 1091.20 Hz, and the corresponding mode shapes are the stage translating in the Y-axis and X-axis, and rotating about the Z axis, respectively.

The comparison between the FEA results and analytical analyses has been carried out and the result is shown in Table III.

According to the above characteristics analysis, it validates that the stage can provide both translational and rotational motions. In addition, the stability of the stage has been improved by the symmetrical arrangement of the T-shape flexure hinge mechanism, and the undesired motions can be avoided. Furthermore, the stage has a high natural frequency, which ensures that the system has good dynamic characteristics.

## 6. Experiment and Results

### 6.1 Controller design

In order to eliminate the hysteresis of PEAs, in this paper, the Bouc-Wen (B-W) hysteresis model is selected as an illustration. It has already been verified that the B-W model is suitable to describe the hysteresis loop of PEA [28-31]. On the other hand, the model is considered in this work since it has fewer parameters. The equation of a B-W model is shown as follows:

$$\dot{h} = ad_e\dot{V}_{pzt} - b\left|\dot{V}_{pzt}\right|h - c\dot{V}_{pzt}\left|h\right| \qquad (29)$$

where $a$, $b$ and $c$ are the parameters of this model, $h$ is the hysteresis variable. And the parameters identification is implemented by nonlinear least square toolbox running in Matlab environment.

Therefore, the inverse B-W model can be cascaded to the physical system as a feedforward hysteresis compensator. The feedback controller is a traditional Proportional-Integral (PI) controller,

which is used to compensate the uncertainty from environment, and improve the stability of the stage. The schematic diagram of the hybrid controller is proposed in Fig. 14.

**6.2 Experiment testing**

The proposed 3-DOF precision positioning stage was manufactured monolithically using wire electrical discharge machining (WEDM) technology, and Al7076 T6 was adopted as the material of the stage. The AE0505D18 PEAs were used with the maximum displacement of 15 μm under the input voltage of 100V. The dSPACE DS1103 controller was used to generate the controlling signal, and the PI E-505.00 amplifier was used to amplify the signal then drive the PEAs. Three KEYENCE laser displacement sensors LK-H050 were used to measure the motion of the stage. Fig. 15 shows the experimental setup for performance measurements.

Figure 16 shows the amplitude of the Frequency Response Function (FRF) of the 3-DOF flexure-based stage. It can be found that the first resonance frequency of the stage is 522.5 Hz, the second and three resonance frequencies are 628.7 Hz and 629.9 Hz, respectively, which are in good agreement with the simulation results. If the PEAs are installed, experiment results show that the first three natural frequencies increase to 805.7 Hz, 810.5 Hz, and 1196 Hz.

As previously mentioned, the motion of the 3-DOF system is coupled. In order to eliminate this shortcoming, the system is controlled in open-loop via inverse kinematics. The control block diagram is presented in Fig. 17. The inverse kinematic matrix is an inverse form of the matrix $\boldsymbol{T}^{-1}$ in the section 4. Therefore, each axis output of the system can be controlled independently when the system is controlled by the simultaneous control of three PEAs. This will make it more convenient applied to the future work.

Fig. 18 depicts the working stroke of PEA under the bolt preload, which is installed in the

stage. Due to the stiffness effect of the flexure mechanism, the actual output displacement of the driving ends is less than the nominal displacement of the PEAs. It can be seen that the stiffness of the preload mechanism has a significant effect on the performance of the PEAs, especially for the working range.

The step responses of the stage are investigated, and the X- and Y- axes step responses are shown in Fig. 19. The result shows that the 2% settling time of the step responses is less than 21 ms. It's noteworthy that the measurement cutoff frequency of the laser displacement sensors are set to 3000Hz.

The motion stroke and coupled motion are also tested, and the result is shown in Fig. 20. It can be seen that the maximum translational displacements in the X- and Y- directions are 6.9 μm and 8.5 μm, respectively, and rotational motion range is 289 μrad. The experimental results are in good agreement of theoretical analyses. As shown in the results, the coupled displacements in the X- and Y- directions are 0.2346 μm and 0.2752 μm, respectively, the cross-axis coupling ratio is below 3.5% ( 3.4% in the X axis, 3.2% in the Y axis), it is mainly due to the assembly errors, manufacture errors and the external disturbances. In this case, the 3-DOF system, which is controlled in open-loop via inverse kinematics can be treated as three Single-Input-Single-Output (SISO) systems.

From Fig. 20, it is also obvious that there are hysteresis phenomena in the motion of the moving platform. Thus, it is crucial to reduce this kind of hysteresis and improve the positioning accuracy of the 3-DOF for the practical applications. Based on the proposed hybrid feedforward/feedback controller, a series of experiments are implemented to verify the performance and effectiveness of the developed control methodology. As can be seen in Fig. 21, the minimum resolutions of 50 nm and 1.25 μrad are clearly resolved from the multi-step response experiment. If

the resolution of the displacement sensor can be improved and the external disturbance signal will be further reduced, a higher resolution of the developed positioning stage can be achieved.

The trajectory tracking of a single 1 Hz sinusoidal input signal in the X and Y axes and a rotation motion about the Z axis are shown in Fig. 22. For the X axis motion, the maximum tracking errors 0.156 μm are observed. And the maximum tracking errors reduce to 0.126 μm in the Y axis motion. The errors are as large as 2.6% and 2.1% with respect to the output displacement in the X and Y axis, respectively. Fig. 16(e) shows sinusoidal trajectories tracking on a rotation motion about the Z axis with the amplitude of 180 μrad. The maximum tracking errors ±5.01 μrad are observed in the motion, which are as large as 2.783% with respect to the angular displacement.

The results of the cross-axis coupling displacement are also obtained in the hybrid controller experiment. The coupled displacements in the X- and Y- directions are 0.175 μm and 0.151 μm, respectively. The cross-axis coupling ratio is 2.91% in the X axis and 2.52% in the Y axis, respectively. This indicates that the proposed closed-loop control methodology can reduce the cross-axis coupling motion and further improve the positioning accuracy.

**7 Conclusions**

This paper presents the design, modeling, characteristic analysis and experimental test of a novel 3-DOF stage. The stage is driven by three PEAs and guided by a flexible mechanism based on three symmetric T-shape flexure hinges. The analytical models of the stage have been established and the stiffness and the dynamic resonance frequency have been obtained. The kinematic model of the 3-DOF stage has been established and the workspace has been calculated. The static and dynamic characteristics of the stage have been verified using FEA, and the flexible hinge-based stage mechanism was manufactured using WEDM technique. Experiments have been conducted to

examine the performance of the stage, and the results show that the stage can provide for excellent static and dynamic performance. The developed stage has the translation motion strokes of 6.9 and 8.5 μm in the X- and Y-axes, respectively, and rotational range of 289 μrad about Z-axis. A hybrid feedforward/feedback control methodology has been proposed to eliminate the nonlinear hysteresis, the trajectory tracking performances and to reduce external disturbance of the 3-DOF stage. The resolutions are 50 nm and 1.25 μrad, respectively, if the resolution of the displacement sensor can be improved and the external disturbance signal will be further reduced, a higher resolution of the developed positioning stage can be achieved. The advantages of the T-shape flexure hinge make this configuration be capable of compact design which is the crucial requirement for small installation space applications such as the chamber of SEM, the fine stage of confocal microscope and AFM.

**Acknowledgement**

This research is supported by National Natural Science Foundation of China (No. 51175372, 51275337), Reserved Academic Program of Peiyang Scholar, and Program for New Century Excellent Talents in University (No. NCET -11-0374).

**References**

[1] J. Paros, L. Weisbord. How to design flexure hinges. Machine Design 1965;37(11):151-156.

[2] Y. Tian, B. Shirinzadeh, D. Zhang. A flexure-based mechanism and control metrology for ultra-precision turning operation. Precision Engineering 2009;33(2):160-166.

[3] T. Tuma, W. Haeberle, H. Rothuizen, J. Lygeros, A. Pantazi and A. Sebastian. Dual-stage nanopositioning for high-speed scanning probe microscopy. IEEE/ASME Transactions on Mechatronics 2014;19(3):1035-1045.

[4] M. Fukuda, M. Hayashi, S. Marita. Generating sub-nanometer displacement using reduction mechanism consisting of torsional leaf spring hinges. Measurement Science Review 2014;14(1):48-51.

[5] Q. Xu. A novel compliant micropositioning stage with dual ranges and resolutions. Sensors and Actuators A:

Physical 2014;205(1):6-14.

[6] Q. Xu. Design and development of a compact flexure-based XY precision positioning system with centimeter range. IEEE Transactions on Industrial Electronics 2014;61(2):893-903.

[7] S. Smith, V. Badami, J. Dale, Y. Xu. Elliptical flexure hinges. Review of Scientific Instruments 2000;68(3):1474-1483.

[8] Y. Tian, B. Shirinzadeh, D. Zhang. Closed-form compliance equations of filleted V-shaped flexure hinges for compliant mechanism design. Precision Engineering 2010;34(3):408-418.

[9] L.L. Howell. Compliant Mechanisms, Wiley, New York, 2001.

[10] B. Trease, Y. Moon, S. Kota. Design of large-displacement compliant joints. ASME Journal of Mechanical Design 2005;127(4): 788-798.

[11] B.D. Jensen, L.L. Howell. The modeling of cross-axis flexural pivots. Mechanism and Machine Theory 2002;37(5):461-476.

[12] M. Goldfarb, J. Speich, The development of a split-tube flexure. The ASME Dynamics and Control Div 2000;2:861-866.

[13] S.T. Smith. Flexures: Elements of Elastic Mechanisms, Gordon and Breach Science, New York, 2000.

[14] S. Venanzi, P. Giesen, V. Parenti-Castelli. A novel technique for position analysis of planar compliant mechanisms. Mechanism and Machine Theory 2005;40(11):1224-1239.

[15] W.O. Schotborgh, F.G. Kokkeler, H. Tragter. Dimensionless design graphs for flexure elements and a comparison between three flexure elements. Precision Engineering 2005; 29(1): 41-47.

[16] X. Pei, J. Yu, G. Zong, S. Bi, H. Su. The modeling of cartwheel flexural hinges. Mechanism and Machine Theory 2009;44(10):1900-1909.

[17] D. Kang, D. Gweon. Analysis and design of a cartwheel-type flexure hinge. Precision Engineering 2013; 37(1):33-43.

[18] T. Takahashi, K. Takada, M. Takeuchi. Light-illuminated STM studies on photo-absorption in InAs nanowires. Ultramicroscopy 2003;97(1-4):1-6.

[19] R. KASSIES, K. O. VAN DER WERF, A. LENFERINK, C. N. HUNTER, J. D. OLSEN, V. SUBRAMANIAM and C. OTTO. Combined AFM and confocal fluorescence microscope for applications in bio-nanotechnology. Journal of Microscopy 2005;217(1):109-116.

[20] Y. K. Yong, S. O. R. Moheimani, B. J. Kenton, and K. K. Leang. High-speed flexure-guided nanopositioning: Mechanical design and control issues. Review of Scientific Instruments 2012;83(12):121101-1-121101-22.

[21] Y. Tian, B. Shirinzadeh, D. Zhang. Design and dynamics of a 3-DOF flexure-based parallel mechanism for micro/nano manipulation. Microelectronic Engineering 2010; 87(2):230-241.

[22] D. Hwang, M. G. Lee, Jaehwa Jeong. Design of a novel ultraprecision in-plane XYθ positioning stage. Review of Scientific Instruments 2011; 82(2): 026102-1-026102-3.

[23] Y. Qin, B. Shirinzadeh, D. Zhang, Y. Tian. Design and kinematics modeling of a novel 3-DOF monolithic manipulator featuring improved Scott-Russell mechanisms. Journal of Mechanical Design 2013;135(10):101004-1-101004-9.

[24] H. Kim and D. Gweon. Development of a compact and long range XYθz nano-positioning stage. Review of Scientific Instruments 2012;83(8):085102-1-085102-8.

[25] U. Bhagat, B. Shirinzadeh, L. Clark, P. Chea, Y. Qin, Y. Tian, D. Zhang. Design and analysis of a novel flexure-based 3-DOF mechanism. Mechanism and Machine Theory 2014;74:173-187.

[26] H. Kim, D. Ahn, and D. Gweon. Development of a novel 3-degrees of freedom flexure based positioning system. Review of Scientific Instruments 2012;83(5):055114-1-055114-11.

[27] Y. Koseki, T. Tanikawa, N. Koyachi, and T. Arai. Kinematic analysis of translational 3-DOF micro parallel mechanism using matrix method. IEEE/RSJ International Conference on Intelligent Robots and Systems(IROS) 2000;1:786-792.

[28] M. Rakotondrabe. Bouc-Wen modeling and inverse multiplicative structure to compensate hysteresis nonlinearity in piezoelectric actuators. IEEE Transactions on Automation and Engineering 2011; 8(2): 428-431.

[29] Y.-T. Liu, K.-M. Chang and W.-Z. Li. Model reference adaptive control for a piezo-positioning system. Precision Engineering 2010; 34(1): 62-69.

[30] J. Park and W. Moon. Hysteresis compensation of piezoelectric actuators: The modified Rayleigh model. Ultrasonics 2010; 50(3): 335-339.

[31] T. S. Low and W. Guo. Modeling of a three-layer piezoelectric bimorph beam with hysteresis. J. MEMS1995; 4(4): 230-237.

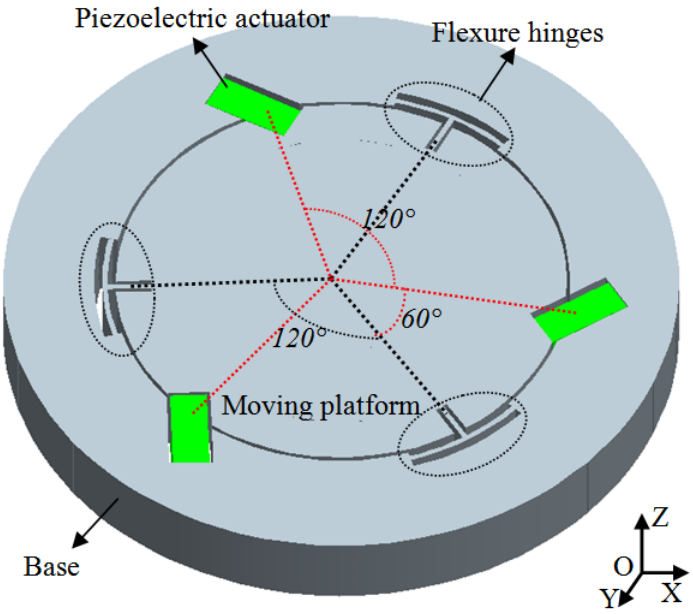


Figure 1 3D solid model of the developed 3-DOF flexure based stage

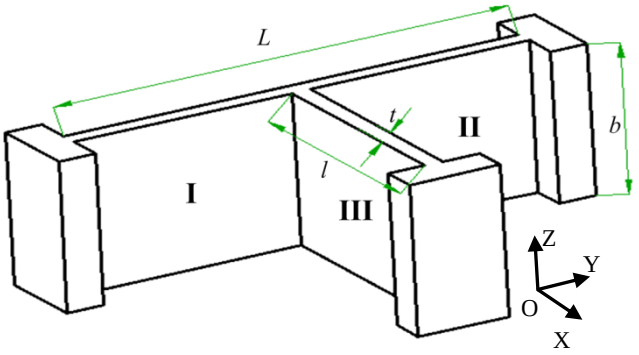


Figure 2 T-shape flexure hinge mechanism.

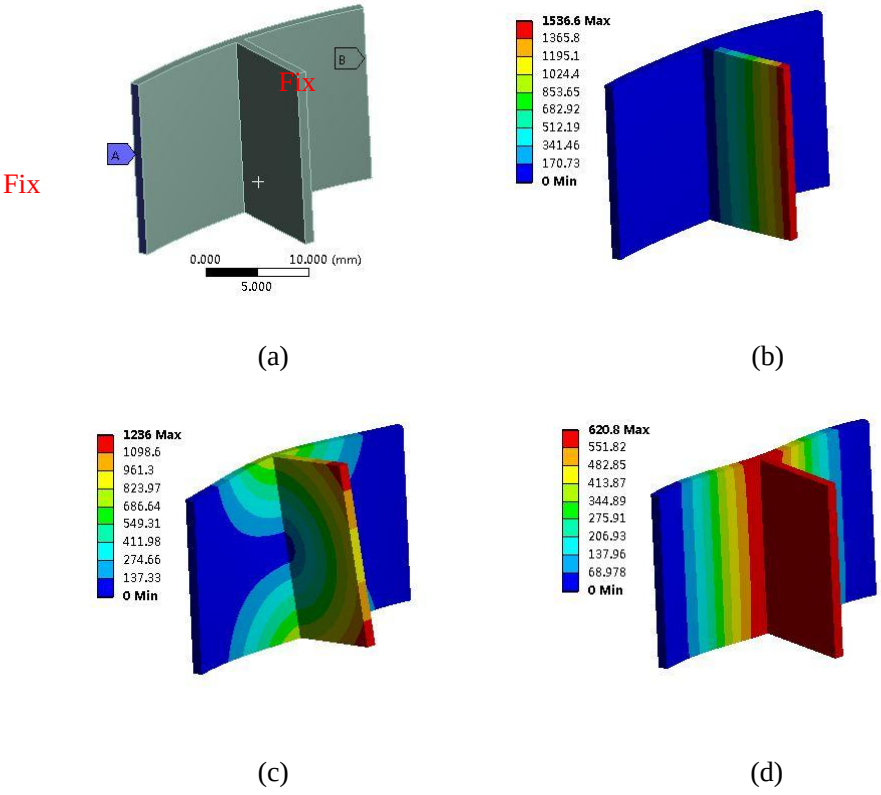


Figure 3 (a) The boundary conditions for simulation, (b) first mode shape (6199.6 Hz), (c) second mode shape (8722.2 Hz) and (d) third mode shape (10197 Hz).

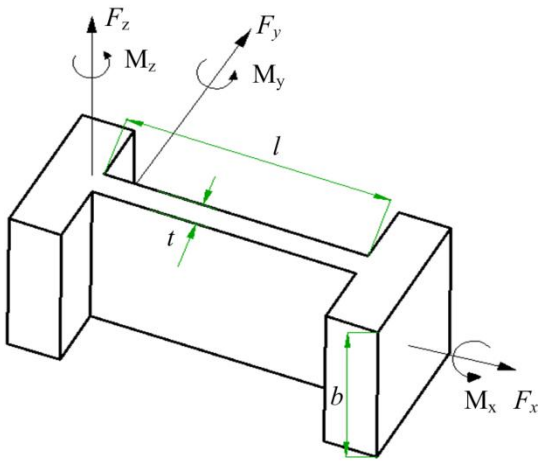


Figure 4 A single leaf-spring hinge.

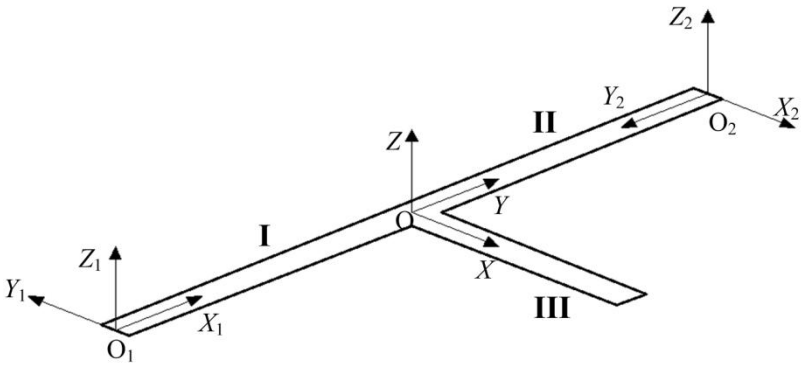


Figure 5 Coordinate systems of the T-shape flexible hinge.

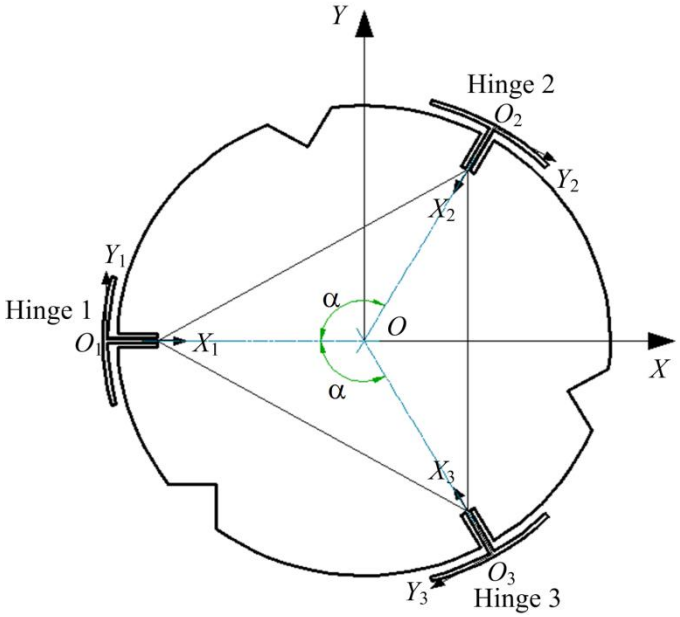


Figure 6 Three T-shape flexible hinges and the moving platform.

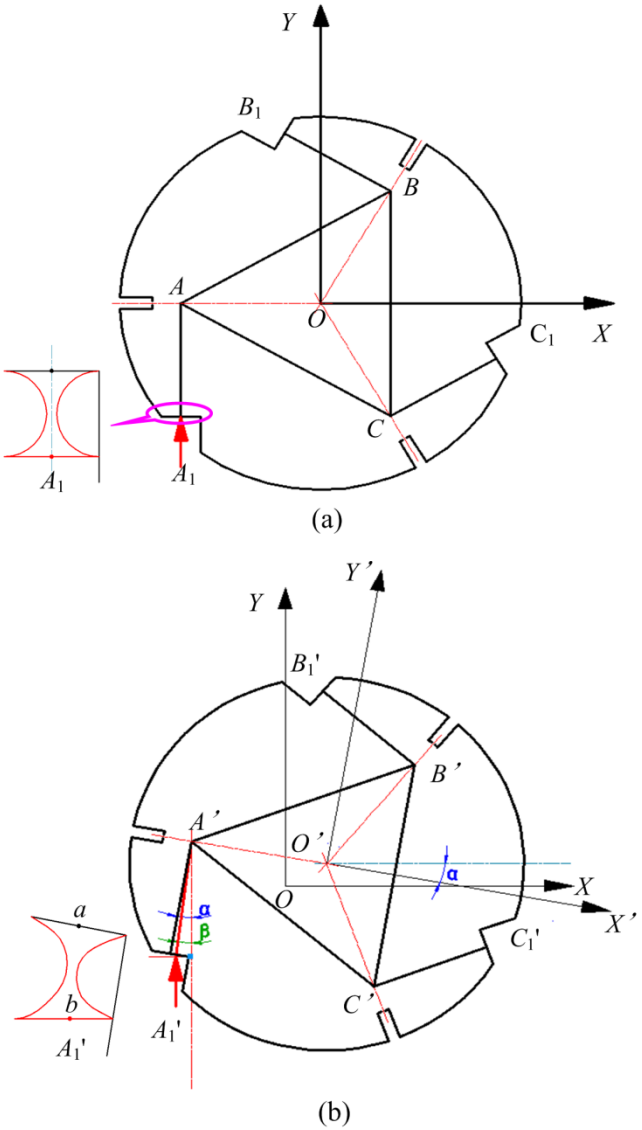


Figure 7 Geometry schematic diagram of the moving platform.

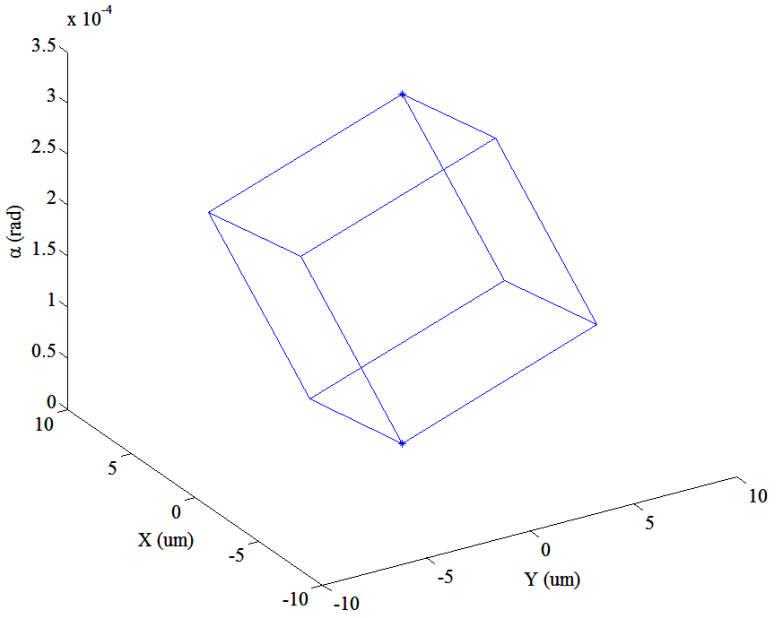


Figure 8 The workspace of the stage (the input displacement δ=12 μm).

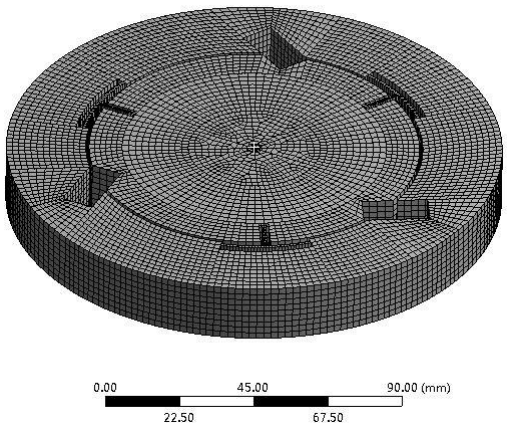


Figure 9 Finite element model of the 3-DOF stage.

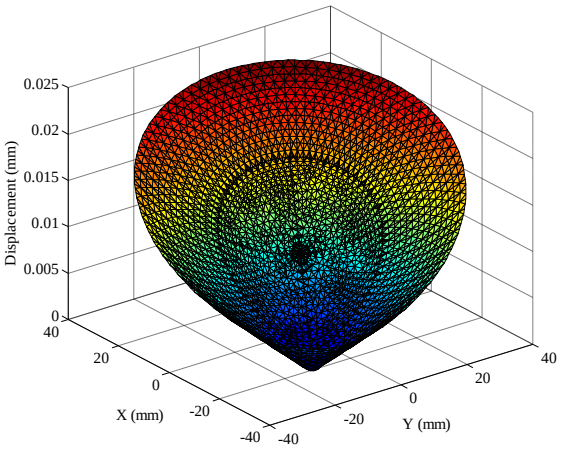


(a) PEA A actuation

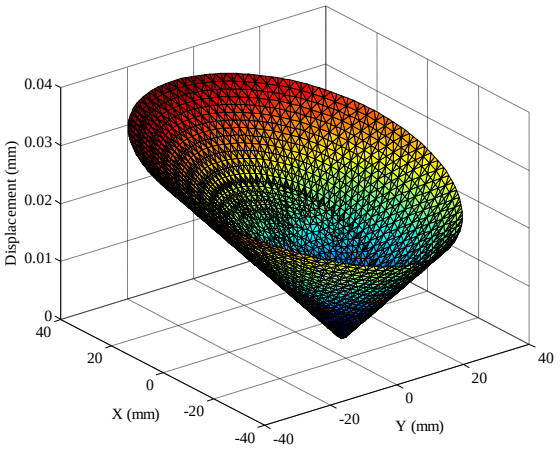


(b) PEAs A and B actuation

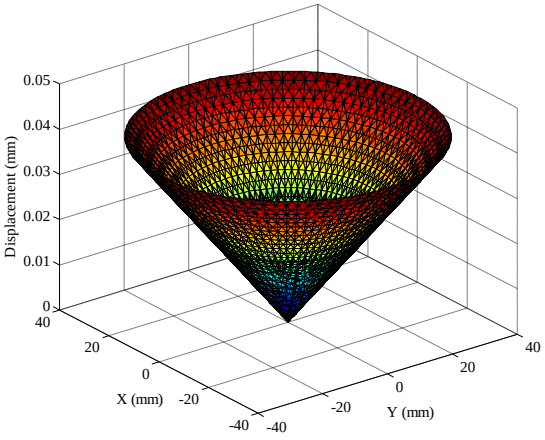


(c) all PEAs actuation

Figure 10 Displacement of the working area.

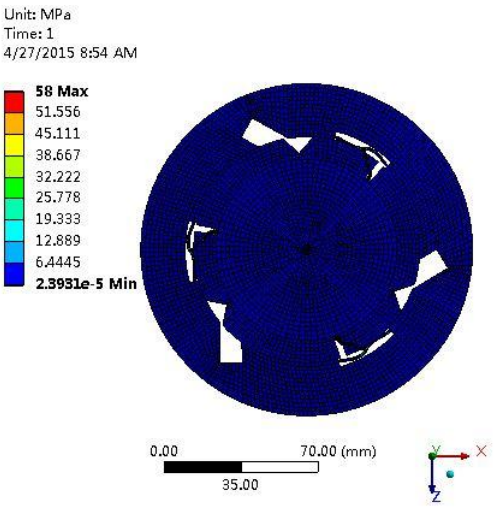


Figure 11 The stress of the hinges.

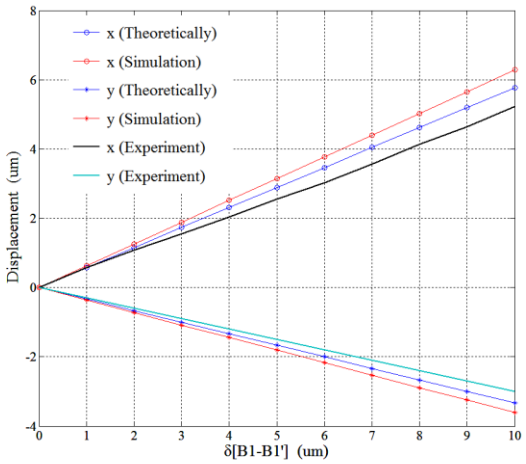


(a) Linear displacements

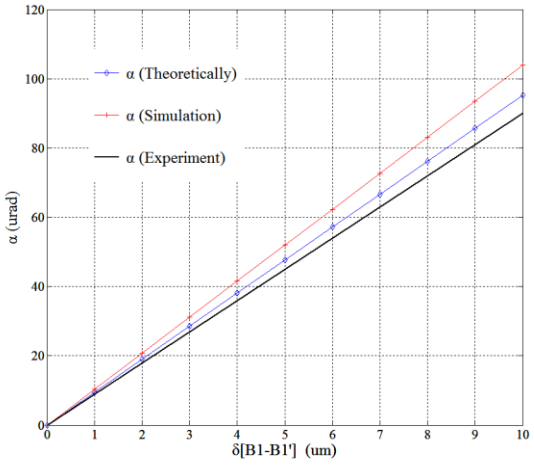


(b) Angular displacement

Figure 12 Response of the moving platform with PEA-B actuation

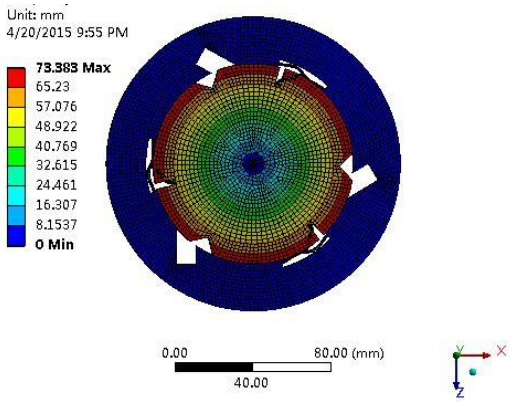


(a)

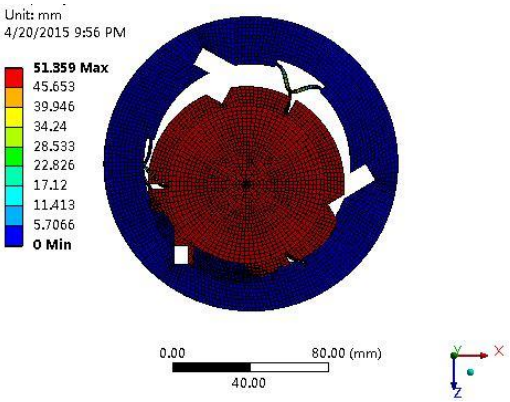


(b)

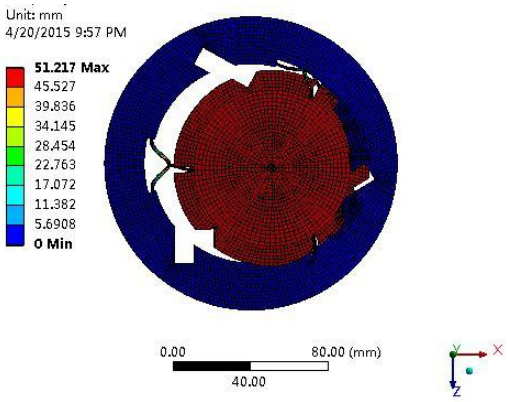


(c)

Figure 13 First three mode shapes of the stage with no PEA installed: (a) first mode shape (528.11 Hz) (b) second mode shape (626.92 Hz) and third mode shape (626.95 Hz).

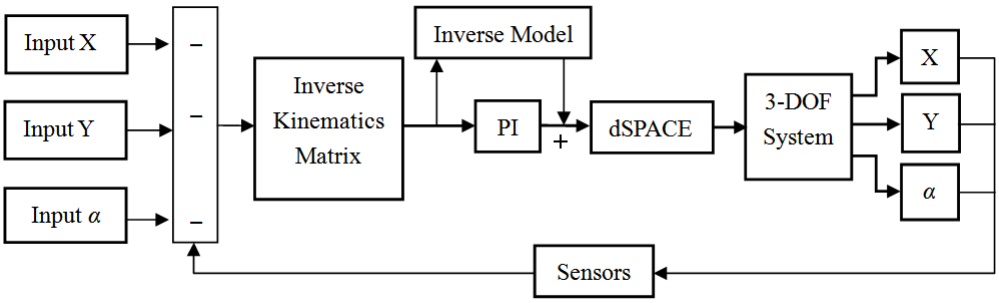


Figure 14 The schematic diagram of the hybrid controller

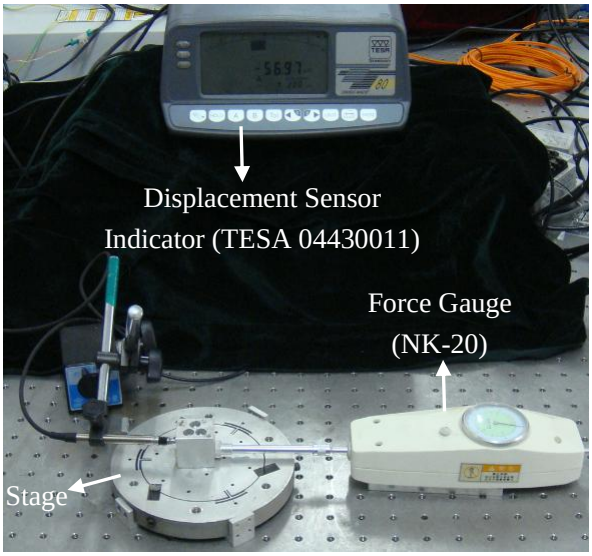


(a) Stiffness measurement

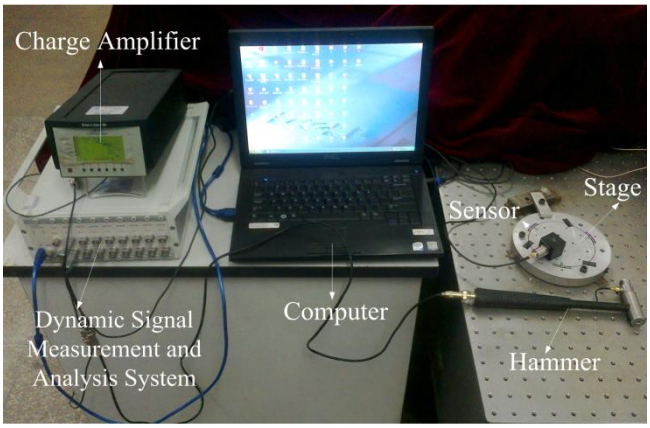


(b) Vibration testing

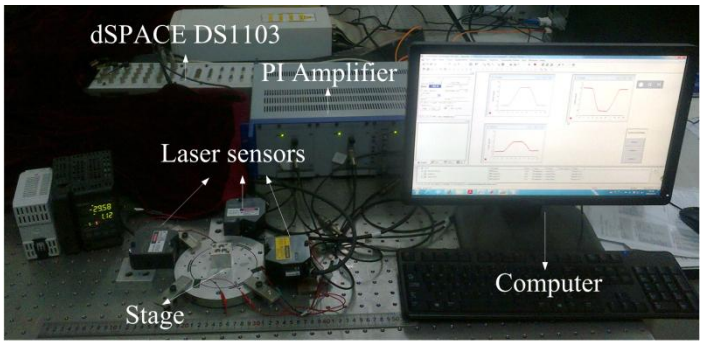


(c) Motion response

Figure 15 Experimental setup of the stage

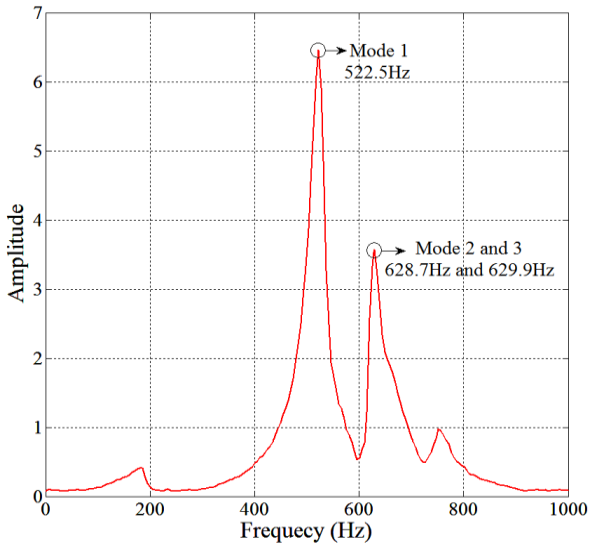


(a) Resonance frequency with no PEA installed

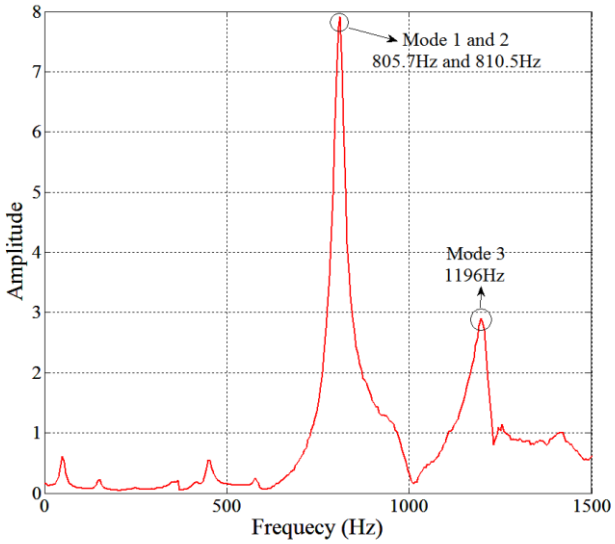


(b) Resonance frequency with PEA installed

Figure 16 Resonance frequency of the stage.

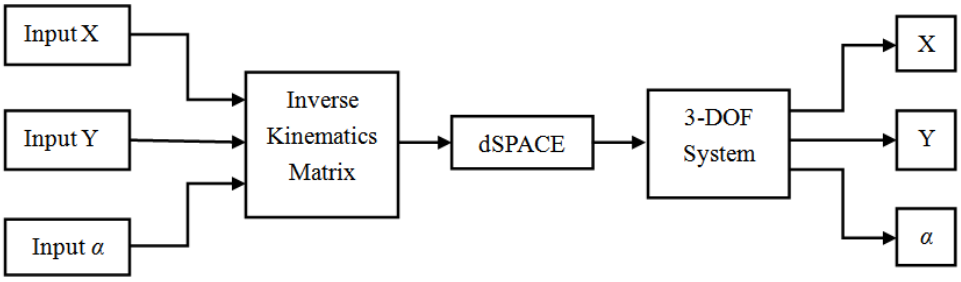


Figure 17 Control block diagram.

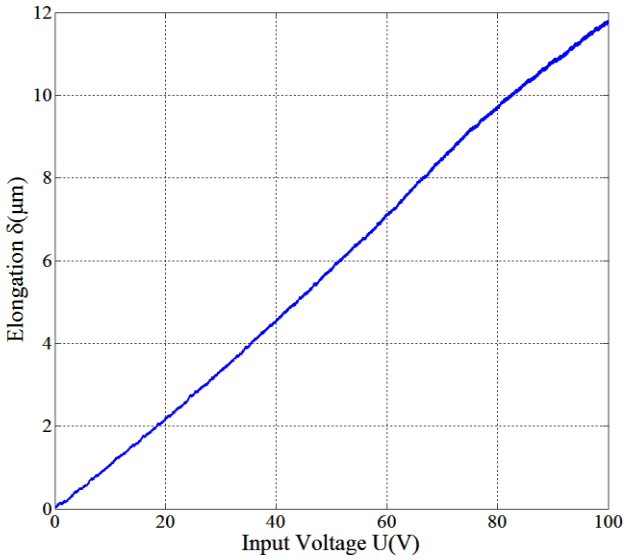


Figure 18 The working stroke test of PEA

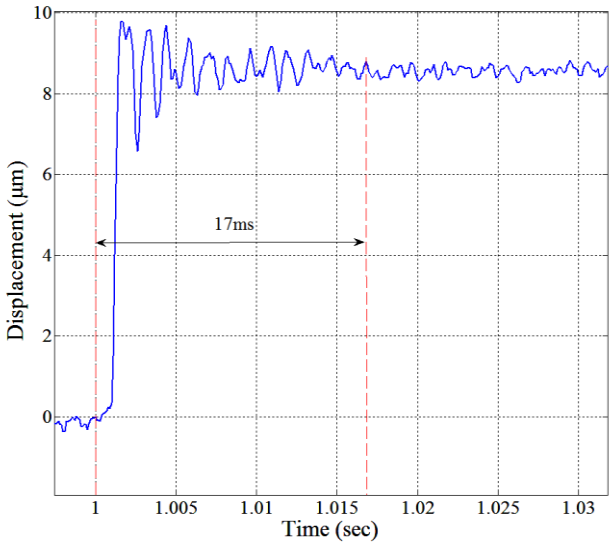


(a) Step response in the X direction

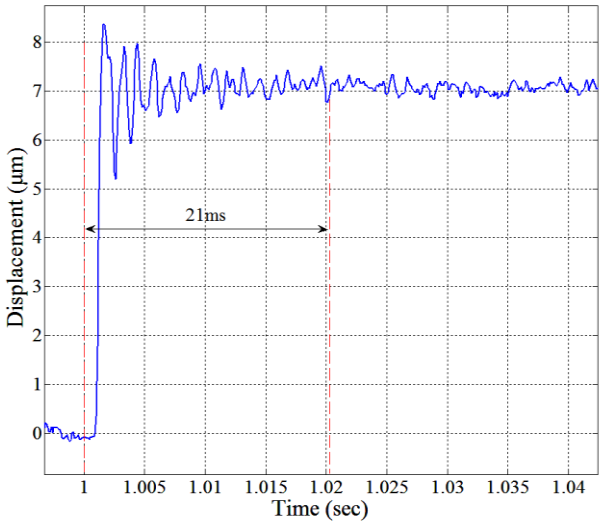


(b) Step response in the Y direction

Figure 19 Step responses of the system (2% settling time).

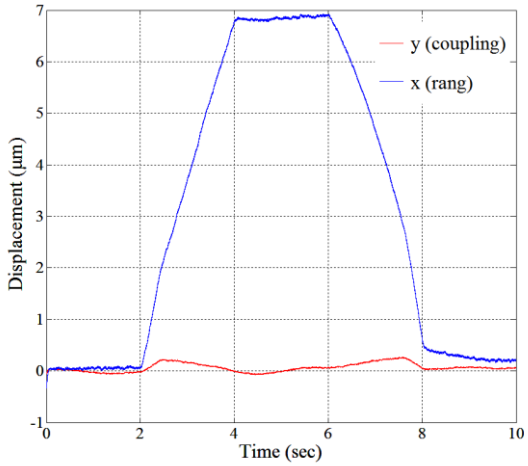


(a)

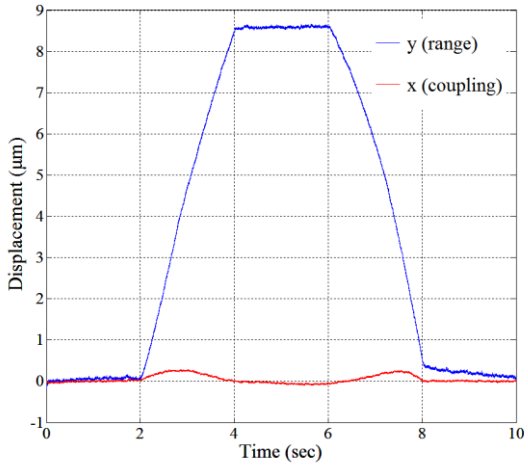


(b)

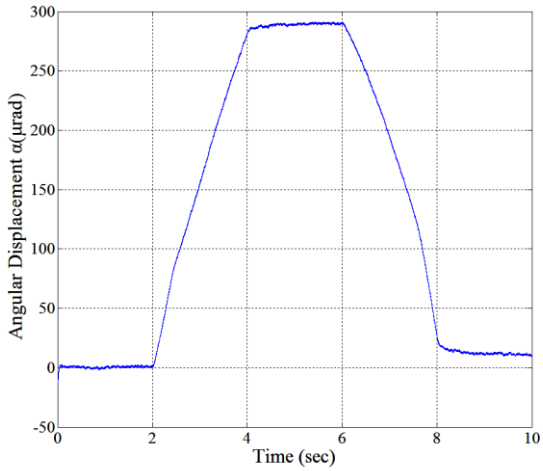


(c)

Figure 20 Experiment test of the motion stroke.

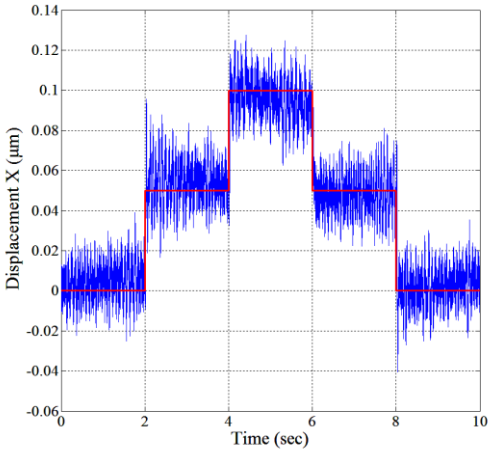


(a)

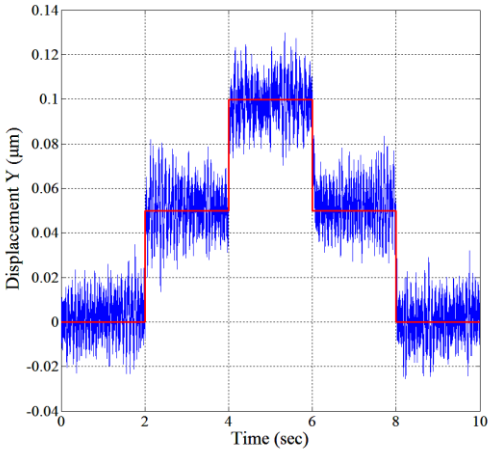


(b)

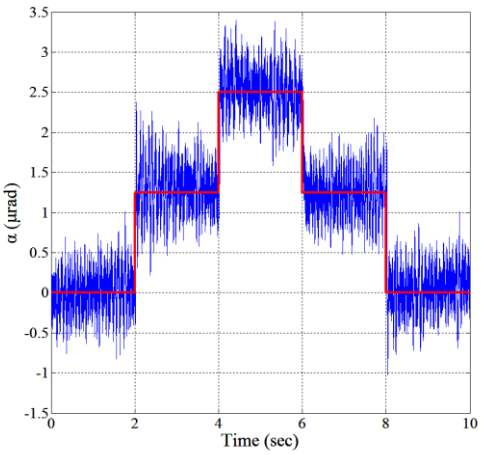


(c)

Figure 21 Multi-step response for the resolution test: (a) X axis, (b) Y axis and (c) $\alpha$ axis.

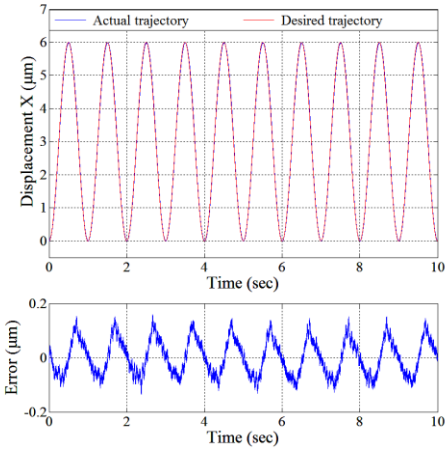


(a)

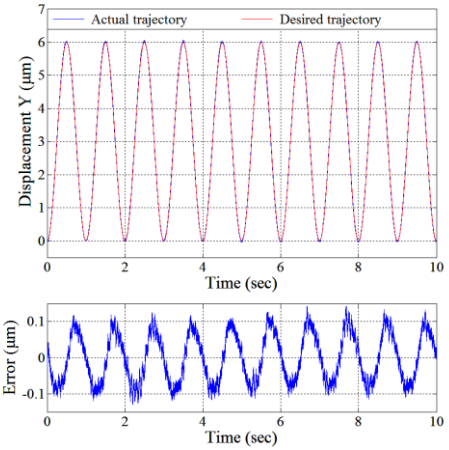


(b)

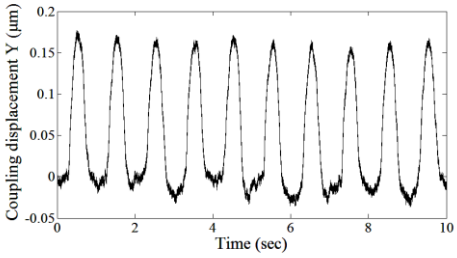


(c)

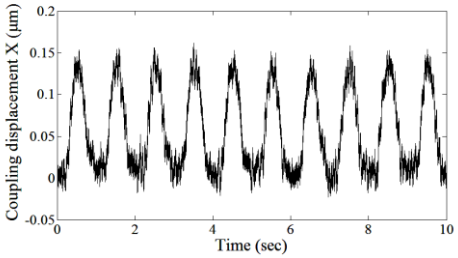


(d)

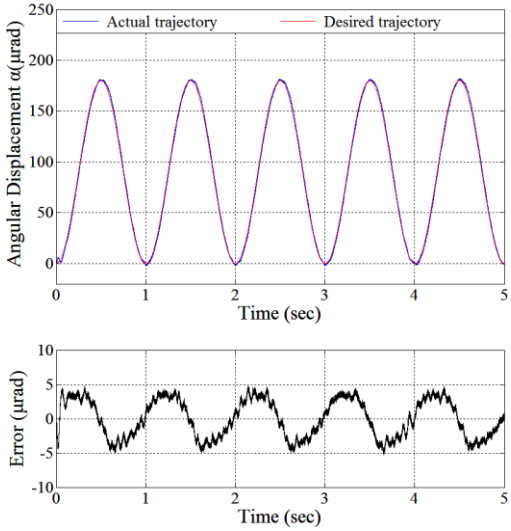


(e)

Figure 22 The result of 1 Hz sinusoidal motion tracking: (a) displacement in the X axis, (b) displacement in the Y axis, (c) coupling displacement in the Y axis, (d) coupling displacement in the X axis and (e) angular displacement about the Z axis.